



HAL
open science

Local energy analysis of HCF fatigue using DIC & IRT

Félix Latourte, André Chrysochoos, Bruno Berthel, André Galtier, Stéphane Pagano, Bertrand Wattrisse

► **To cite this version:**

Félix Latourte, André Chrysochoos, Bruno Berthel, André Galtier, Stéphane Pagano, et al.. Local energy analysis of HCF fatigue using DIC & IRT. SEM 2009, Jun 2009, Albuquerque, United States. pp.Cd-Rom. hal-00836156

HAL Id: hal-00836156

<https://hal.science/hal-00836156>

Submitted on 20 Jun 2013

HAL is a multi-disciplinary open access archive for the deposit and dissemination of scientific research documents, whether they are published or not. The documents may come from teaching and research institutions in France or abroad, or from public or private research centers.

L'archive ouverte pluridisciplinaire **HAL**, est destinée au dépôt et à la diffusion de documents scientifiques de niveau recherche, publiés ou non, émanant des établissements d'enseignement et de recherche français ou étrangers, des laboratoires publics ou privés.

LOCAL ENERGY ANALYSIS OF HIGH-CYCLE FATIGUE USING FIELD MEASUREMENTS

F. Latourte¹, A. Chrysochoos², B. Berthel³, A. Galtier⁴, S. Pagano², B. Wattrisse²

¹ Northwestern University, Dept. of Mechanical Engineering, 2145 Sheridan Road, Evanston IL 60201, USA, f-latourte@northwestern.edu

² University of Montpellier II, Mechanics and Civil Engineering Laboratory

³ Ecole Centrale de Lyon, Laboratory of Tribology and Systems Dynamics

⁴ French Industrial and Mechanical Technical Centre

ABSTRACT

We present here an experimental setup developed to locally estimate the terms of the energy balance associated with high cycle fatigue (HCF) of DP 600 steel. Our experiments involve two quantitative imaging techniques: digital image correlation (DIC) and infrared thermography (IRT). Kinematics fields obtained by DIC allow the estimation of stress and energy density fields by means of a variational method. The temperature recorded by IRT is used to resolve a local form of heat equation, giving thermoelastic and dissipative sources accompanying HCF. Our first results show that around 50% of the deformation energy associated with the mechanical hysteresis loop is dissipated while the rest corresponds to stored energy variations

KEYWORDS: Image correlation, thermography, deformation work, dissipation, stored energy, fatigue, steel

1 - INTRODUCTION

It is well known that standard characterization of fatigue in materials requires time-consuming and statistical processing of the numerous results provided by expensive mechanical tests. Over the last two decades, alternative experimental approaches have been developed to rapidly produce reliable fatigue characteristics, including thermal methods based on the analysis of self-heating during stepwise loading fatigue tests [1-2]. Although realistic estimates of these characteristics have sometimes been obtained, the thermal approach often leads to questionable results [3]. The direct use of temperature as a fatigue indicator may not always be the most relevant approach since the temperature variation is not intrinsic to the material behaviour [4].

During high cycle fatigue, a first part of the calorimetric energy is induced by irreversible manifestations of microstructural defects, and another part is coming from thermoelastic coupling sources linked to the reversible thermal expansion of the crystalline network. Here we could compare deformation and dissipated energies to indirectly estimate the energy stored by the material during HCF. An improved combined image processing was developed to obtain 2D patterns of energy balances. Speckle image correlation techniques, involving a charge-coupled device (CCD) camera [5], were used to assess surface displacement fields. In parallel, thermal data were provided by an infrared focal plane array (IRFPA) camera [6]. Heat sources were estimated on the basis of partial derivative operators present in a local form of the heat diffusion equation using a set of approximation functions that locally fits the temperature field and takes the spectral properties of the sought sources into account.

Considering the stored energy variations is of prime interest since they correspond to internal energy variations induced by microstructural transformations. Generally speaking, these variations and those of thermoelastic sources are directly linked to the thermodynamic potential chosen to describe the material state. Furthermore, experimental dissipation data give valuable information to define a consistent dissipation potential used to derive the evolution laws describing the irreversibility of the fatigue process. Stored and dissipated energies are finally essential safeguards to formulate thermomechanically consistent constitutive equations for the fatigue model.

The paper is composed as follows: the different terms of the energy balance associated with high cycle fatigue of steels are first recalled. A brief review of kinematical and thermal image processing principles is then given and the benefits of their combined use underlined. Finally, 2D energy fields obtained on dual-phase steel (DP600) are presented to highlight the promising character of this local energy analysis of fatigue mechanisms.

2 - LOCAL FORM OF THE ENERGY BALANCE

From a thermomechanical point of view, fatigue is considered as a dissipative quasi-static process. Within the formalism of the classical irreversible processes Thermodynamics [7], the equilibrium state of each volume material element is then described using a set of N state variables. The chosen variables are: the absolute temperature T , the linearized strain tensor ϵ (small strain hypothesis) and $N-2$ element vector α which pools the so-called internal variables. These variables describe the macroscopic effects of complex coupled microstructural phenomena.

The rate of deformation energy w^*_{def} is classically defined by:

$$w^*_{def} = \sigma : \dot{\epsilon} \quad (1)$$

where σ is the Cauchy stress tensor. The symbol $()^*$ means that the time variation of $()$ is path-dependent (e.g. w_{def} is not a state function a priori). The local heat diffusion equation is written as:

$$\rho C \dot{T} - \text{div}(K \text{grad}T) = d_1 + s_{the} + s_{ic} + r_{ext} \quad (2)$$

where ρ is the mass density, C the specific heat, K the conduction tensor. The heat sources are, in turn, the intrinsic dissipation d_1 , the thermomechanical coupling sources that pool the thermoelastic source s_{the} and the other internal coupling sources s_{ic} , and the external volume heat supply r_{ext} . The volume heat sources d_1 , s_{the} and s_{ic} are related to the specific free energy $\psi(T, \epsilon, \alpha)$ by:

$$\begin{cases} \text{(a)} & d_1 = \sigma : \dot{\epsilon} - \rho \psi_{,\epsilon} : \dot{\epsilon} - \rho \psi_{,\alpha} \cdot \dot{\alpha} \\ \text{(b)} & s_{the} + s_{ic} = \rho T \partial^2 \psi / \partial T \partial \epsilon : \dot{\epsilon} + \rho T \partial^2 \psi / \partial T \partial \alpha \cdot \dot{\alpha} \end{cases} \quad (3)$$

Equation (3a) means that the intrinsic dissipation is the difference between the deformation energy rate and the sum of the elastic and stored energy rates. The second-order cross derivatives of the free energy in Equation (3b) underlines the thermo-dependence of the material which induces coupling heat sources. During our fatigue tests, temperature variations remained minimal (< 15 K) and could not modify the internal state of the material, so we neglected the corresponding heat sources s_{ic} and the thermoelastic sources were compared with the ones given by the classical linear thermoelastic model. The thermoelastic source could then be written as $s_{the} \approx -\alpha_d T_0 \text{tr} \dot{\sigma}$, where α_d is the linear thermal expansion coefficient and “tr” stands for the trace operator and where T_0 is the room temperature.

3 □ LOCAL ENERGY ASSESSMENT

3.1 - Deformation energy

To compute the deformation energy, we used a DIC technique to obtain the space-time evolution of in plane components of the displacement on the sample surface. The camera used was a Camelia 8M, able to acquire 5 frames per second, and we used white light to illuminate the sample. Distortions were minimized by aligning carefully the camera to set the CCD detector parallel to the monitored area. The comparison between strain fields associated with rigid body motions and the strain measurements enabled us to check and optimize the alignment procedure. Strains (or the strain-rates) were then derived from the displacements by space (and time) differentiation. To control differentiation errors, the displacement field was filtered before differentiation, using a local least-squares approximation of the discrete displacement data. The choice of the approximation zone (AZ) determines the quality of the differentiation process. The optimized AZ depends on the signal-to-noise ratio and the amplitude of the sought derivatives. In the case of the fatigue tests described hereafter, the absolute uncertainty in terms of displacement measurement was about 5×10^{-2} pixels and 1×10^{-4} regarding the strain

calculation. The reader, interested in the detailed metrological issues of the image processing used in this work, can refer to [5]. Measurement fields were obtained on surfaces totally covering the sample gauge part. The specimen retained for this study was a classical flat dogbone tensile specimen of thickness 2.6mm, and having a 10mm x 10mm gauge part. An extended region of interest was monitored in this study, in which the x coordinate ranged from -10 to 10mm (see Figure 2).

A variational method, associated with an elastic energy functional, defined by [8] was used both to identify the field of elastic parameters and to determine the elastic stress pattern σ . The micro-plastic and micro-damage effects induced by HCF were then supposed to be taken into account by performing an elastic identification at each loading step. By doing so, we admitted that the stress field at mesoscopic scale remains close to the elastic one for a given overall loading and a given strain field. The energy functional F on an appropriate domain of interest Ω (typically the sample gauge part) reads:

$$F(\tau, B) = \frac{1}{2} \int_{\Omega} (\varepsilon(u) - B : \tau) : B^{-1} : (\varepsilon(u) - B : \tau) d\Omega \quad (4)$$

A minimisation of F performed numerically by a relaxation method gives the stress field solution and the field of elastic parameters, respectively. During the tests, the overall forces applied at the specimen boundary were recorded. For each loading step, the variational approach provided a couple (σ, A) where σ is a stress tensor and A a compliance tensor. This couple becomes a candidate solution to the identification problem if it satisfies local equilibrium equations, linear elasticity equations and global equilibrium.

Knowledge of the stress and strain-rate fields then allows constructing distributions of deformation energy rate. To estimate w_{def}^{\bullet} , we used the in-plane components (U, V) of the displacement field and neglected the influence of temperature. The plane stress hypothesis was supposed to be valid until strong triaxiality effects induced by fatigue localization occur. This time-consuming operation led to a slight, regular adjustment of elastic parameters enabling us to describe the mechanical hysteresis loop.

To check the consistency of the results given by the variational approach, plane stress components were also computed using local equilibrium equations and strain data as in [9]. We observed that both approaches give similar results. An order of magnitude of the mean relative uncertainty between both types of estimate is about 75 kJ.m^{-3} for a mean deformation energy rate per cycle of about 1 500 kJ.m^{-3} , (see [10] for more details).

Then, stress and strain field measurements were used to compute the mean volume energy rate corresponding to the hysteresis A_h :

$$A_h(x, y) = \int_0^{f_l^{-1}} \sigma_{ij}(x, y, t) \dot{\varepsilon}_{ij}(x, y, t) dt = w_{def}(x, y) \quad (5)$$

where f_l is the loading frequency. The hysteresis area indeed represents the deformation energy finally spent in a cycle at given fatigue state (*i.e.* a given number of cycles – or a given block of cycles– for given loading history).

3.2 □ Heat sources

The Cedip Jade 3 IRFPA camera was calibrated using a planar black body SR 80-4A (by CI Systems). Standard calibrations are based on a non uniformity correction (NUC operation) that supposes a linear response of each detector element [6]. A main feature of this correction is the bad pixel replacement (BPR), which may distort the thermal gradient computation by spatially correlating measurement errors. To reduce measurement artefacts, a new protocol based on individual calibration of detector elements has been proposed that shortcuts NUC and BPR operations. Additional details about these challenging metrological issues can be found in [6]. We estimated here that the peak-to-peak thermal noise was about 200 mK (*i.e.* before data filtering) and the range of the thermal noise dropped to 2 mK for standard filtering parameters. The filtering procedure involves a fitting of temperature data using approximations functions described in Eq.(7). Moreover, the order of magnitude of the spatial resolution was about 0.16 mm and the temporal resolution was considered to be equal to the 0.05 s acquisition period used in the fatigue tests.

The overall heat source can be theoretically estimated by evaluating the left-hand side of the heat equation (Eq.(2)). Nevertheless, the only thermal information given by the IR camera is surface temperature fields. The heat source evaluation throughout the specimen gauge part (3D inverse problem) is an ill-posed problem that is impossible to solve without any complementary information.

The regularizing effects of heat diffusion fortunately limit the thermal gradients throughout the (small) thickness of the specimen. In particular, we previously established that thermal data on the surface remain close to the average temperature during cyclic tests [6].

This result warranted the use of an integrated form of the heat equation over the sample thickness to estimate the depth-wise averaged heat source distribution. The following assumptions were also made to perform the heat source evaluation: (i) the conduction tensor K is isotropic and the related coefficient k remains constant during the test; (ii) parameters ρ and C are material constants, independent of the internal state; (iii) the convective terms included in the material time derivation are neglected; (iv) the external heat supply r_{ext} (here only due to radiation heat exchanges) is time-independent. Consequently, the equilibrium temperature field T_0 verifies $-k\Delta T_0 = r_{\text{ext}}$.

While temperature variations $\theta = T - T_0$ induced by fatigue mechanisms remain small, we admit that they have no influence on the microstructural state. It can therefore be stated that $s_{\text{ic}} = 0$.

Under these hypotheses, the following 2D equation can be obtained:

$$\rho C \left(\frac{\partial \bar{\theta}}{\partial t} + \frac{\bar{\theta}}{\tau_{\text{th}}} \right) - k \Delta \bar{\theta} = \bar{d}_1 + \bar{s}_{\text{the}} \quad (6)$$

(i) assuming symmetrical linear heat exchanges between the front/back specimen faces and the surroundings, (ii) integrating Eq. (2) over the sample thickness, (iii) assuming that the thermal image is very close to the depth-wise averaged temperature field. In Eq.(6), $\bar{\theta}$ is the depth-wise averaged temperature variations, k is the isotropic conduction coefficient, \bar{d}_1 and \bar{s}_{the} are the dissipation and thermoelastic source averaged over the sample thickness, respectively. The symbol τ_{th} stands for a time constant characterizing heat losses perpendicular to the plane of the specimen, while heat conduction in the plane is taken into account by the two-dimensional Laplacian operator Δ .

Construction of the heat source distribution *via* equation (6) requires the evaluation of partial derivative operators applied to noisy digital signals. To compute reliable estimates of heat sources, it is then necessary to reduce the noise amplitude without modifying the spatial and temporal thermal gradients. Among several possible methods, a special local least-squares fitting of the thermal signal was considered for the calorimetric fatigue analysis [4, 6, 11]. The temperature approximation functions account for the spectral properties of the underlying heat sources. Moreover, the linearity of equation (3) and that of the respective boundary conditions enabled us to separately analyze the influence of thermoelastic and dissipative heat sources. Moreover, within the linear thermoelasticity framework, it is easy to verify that:

- the thermoelastic source has the same frequency spectrum as the stress signal;
- the variation in the thermoelastic energy w_{the} vanishes at the end of each loading cycle of period f_L^{-1} .

Regarding the dissipative effects, we have considered the dissipation averaged over a whole number n of complete cycles (e.g. $n \sim$ number of cycles per second) $\tilde{d}_1 = \int_n f_L^{-1} n^{-1} f_L \bar{d}_1 d\tau$.

The new variable \tilde{d}_1 is sufficient to characterize the slow changes of the material microstructure due to fatigue phenomena. The average dissipation per cycle \tilde{d}_1 is thus a positive heat source whose spectrum is limited to very low frequencies.

Henceforth by denoting $\bar{\Delta s}_{\text{the}}$ as the range of the thermoelastic source averaged over n cycles, the aim of the image processing is to separately assess $\bar{\Delta s}_{\text{the}}$ and \tilde{d}_1 .

The local fitting function θ^{fit} of the temperature charts was chosen as:

$$\theta^{\text{fit}}(x, y, t) = p_1(x, y)t + p_2(x, y) + p_3(x, y)\cos(2\pi f_L t) + p_4(x, y)\sin(2\pi f_L t) \quad (7)$$

where the trigonometric time functions describe the periodic part of the thermoelastic effects while the linear time function takes transient effects due to heat loss, dissipative heating and possible drift in the equilibrium temperature into account. Functions $p_i(x, y)$, $i = 1, \dots, 4$, are 2nd order polynomials in x and y . These polynomials enabled us to take possible spatial heterogeneities in the source patterns into account. Calibration results show that the approximation function set is convenient to correctly construct a denoized temperature signal.

The linearity with respect to temperature of Equation (6) and that of the respective boundary conditions enabled us to separately analyze the influence of thermoelastic and dissipative heat sources. The energy variables derived from the thermal image processing were finally \tilde{d}_1 the mean dissipated energy per cycle and $\bar{\Delta s}_{\text{the}}$ the

mean amplitude of thermoelastic effects, averaged over n complete loading cycles. The first characterizes the slow degradation of the material microstructure due to fatigue phenomena including diffuse microplasticity, development of localized persistent slip bands, and progressive damage growth leading to microcracks while the second is associated with the reversible thermo-dilatibility of the material and should indicate possible interactions between microplasticity, fatigue damage and elastic properties.

4 - EXPERIMENTAL RESULTS

The material under examination is DP600 steel produced by Arcelor Mittal (Dual Phase Carbon Steel). This material is a hot-rolled steel grade containing ferrite and martensite. The thermophysical properties of DP600 are the following: mass density $\rho=7800 \text{ kg.m}^{-3}$, heat capacity $C=460 \text{ J.kg}^{-1}.\text{K}^{-1}$, isotropic heat conduction coefficient $k=64 \text{ W.m}^{-1}.\text{K}^{-1}$, linear thermal expansion coefficient $\alpha_d=10 \cdot 10^{-6} \text{ K}^{-1}$. The standard mechanical properties are the following: Young's modulus $E= 213 \text{ GPa}$, yield stress $\sigma_{0.2\%} = 401 \text{ MPa}$, ultimate tensile stress $\sigma_u = 611 \text{ MPa}$. The fatigue limit obtained at $2 \cdot 10^6$ cycles for a loading ratio $R_\sigma = \sigma_{\min}/\sigma_{\max} = -1$ is about $\Delta\sigma_{\text{inf}} = 526 \pm 5 \text{ MPa}$.

The tests involved two series of five short loading blocks ($N_c=2 \cdot 400$ cycles) performed at increasing stress range $\Delta\sigma$ ($180 \text{ MPa} < \Delta\sigma < 570 \text{ MPa}$) with a constant stress ratio $R_\sigma = -1$ and a constant loading frequency $f_L=30 \text{ Hz}$. Between the two series, a block of 100 000 cycles was completed with the maximal stress range nearly corresponding to the fatigue limit. Figure 1 illustrates the sequences of blocks associated with the test. The shorter blocks allowed estimating the dissipation levels at different stress amplitudes and at relatively constant damage state whereas the longer block – at maximal constant stress range – aimed at speeding up the fatigue development. At the end of each block, a cycle was completed at a lower loading frequency ($f_L=5.55 \cdot 10^{-3} \text{ Hz}$). During this last cycle, displacement fields were then provided for the identification procedure determining local elastic tensors, and plane stress patterns. In addition, the calorimetric analysis showing that the energy dissipated in a cycle was independent of the loading frequency [11,12], we assumed that the deformation energy corresponding to the hysteresis loop of the stress-strain curve was also rate-independent. It should be underlined that this important hypothesis is fully consistent with a thermoelastic-plastic-damageable behaviour.

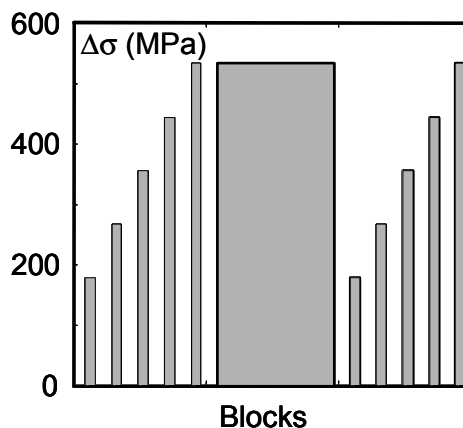


Fig. 1: Series of blocks: short blocks = 2400 cycles, long block = 100 000 cycles.

4.1 Identification of elastic parameters and stress patterns

First, the results derived from the identification procedure are presented. Using the variational inverse method, we obtained the distribution of elastic parameters. We estimated that for load levels lower than the threshold load $F_{\min}=2.5 \text{ kN}$ and corresponding to a macroscopic strain level of $4 \cdot 10^{-4}$, comparable to the resolution of the strain measurement, the identified material properties could not be estimated precisely. For higher load levels, the identified values were stable. Averaging the representative values over the loading cycle, we obtained: $\langle E \rangle_{\text{cycle}}=215 \text{ GPa}$ and $\langle \nu \rangle_{\text{cycle}}=0.3$. While comparing the averaged elastic moduli between blocks, no clear influence of fatigue damage on the elastic parameters was found [13]. During loading cycles, slight and regular variations of the identified elastic moduli can be observed. These variations were interpreted as the result of couplings between elasticity and microplasticity slightly modifying the identified secant compliance tensor.

Figure 2(a-b) shows fields of elastic properties identified after the 11th block and averaged over the loading cycle for $|F| \geq F_{\min}$. The material coefficients are determined on a regular mesh constituted by 10×10 elements centered in the middle of the sample gauge part.

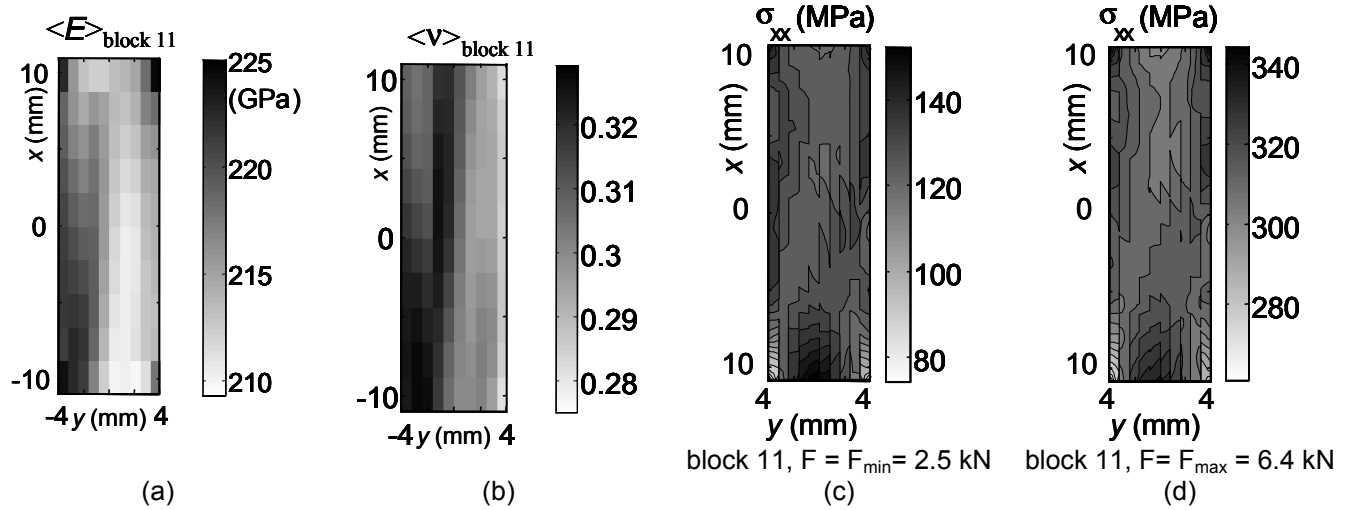


Fig. 2: Averaged elastic parameters over a loading cycle: (a) Young's modulus associated with block #11, (b) Poisson's ratio associated with block #11. Tensile component of plane stress patterns captured at F_{\min} (c) and F_{\max} (d) for the same block.

The distributions of elastic parameters are quite homogeneous: standard deviations are smaller than 4 GPa on Young's modulus and 0.014 on Poisson's ratio. This represents around 5% of spatial variations. Nevertheless, these small variations look like deterministic gradients since similar patterns of identified parameters are derived throughout the test. This can be verified by comparing the evolution of the identified patterns at different blocks. The noisy nature of displacement data and the unstable character of inverse methods lead to interpret identification results with care. Although steady gradients of material properties may come from uncontrolled, systematic errors of the image processing, they could likely be connected to the heterogeneity of the material state. The knowledge of the initial heterogeneity of the material state is thus becoming essential to improve understanding and mastering of the random response of fatigue specimens which led several authors to model high cycle fatigue as random phenomena (e.g.[14-15]). Supplementary tests have to be developed to check the reliability of this key conjecture.

The identification method also provided the plane stress distributions which are essential to compute the deformation energy associated with a mechanical hysteresis loop. Figure 2(c-d) shows distributions of the tensile component of the plane stress field, captured at F_{\min} (yield load) and F_{\max} (maximum load) of the cycle associated with the 11th block. We also could notice that transversal (σ_{yy}) and shear (σ_{xy}) stresses remained low compared with the tensile stresses (σ_{xx}) as expected for a so-called uniaxial tensile test [13]. Furthermore, stress patterns are very similar regardless of the applied load (F_{\min} , F_{\max}) within the same block, and additional results can show similarities between blocks. This feature is in agreement with the identification of the elastic parameters in the sense that stress patterns seem to be independent of the loading history and then might account for the material heterogeneity.

4.2 □ Analysis of energy balances

Preliminary 2D energy fields obtained by using both imaging techniques are now presented. Dividing volume energy by volume heat capacity ρC of the material gives volume energy expressed in $^{\circ}\text{C}$. This operation is convenient because it associates an equivalent heating in adiabatic conditions and then gives order of magnitudes of this energy in unit easy to grasp. The deformation energy on a cycle was computed by using the stress and strain data (see Equation (5)). The distribution of dissipated energy was averaged over the last 120 cycles of the block. We already mentioned in [4] that these averaged values are representative of the slow development of irreversible fatigue phenomena.

The stored energy is defined as the difference between the deformation energy spent in a cycle and the energy dissipated during this cycle: Indeed, we mentioned that Equation (3) shows that intrinsic dissipation d_1 is the difference between deformation energy rate w_{def}^{\bullet} and the sum of the elastic and stored energies $w_e^{\bullet} + w_s^{\bullet}$:

$$d_1 = \underbrace{\sigma : \dot{\varepsilon}}_{w_{\text{def}}} - \underbrace{(\rho \partial \psi / \partial \varepsilon : \dot{\varepsilon} + \rho \partial \psi / \partial \alpha : \dot{\alpha})}_{w_e^* + w_s^*} \quad (8)$$

Integrated over a complete loading cycle, Equation (8) shows that the deformation energy w_{def} can be split into the dissipated energy w_d and the stored energy w_s , the elastic energy w_e vanishing at the end of each load-unload cycle. Figure 3 shows the energy balance associated with block #11.

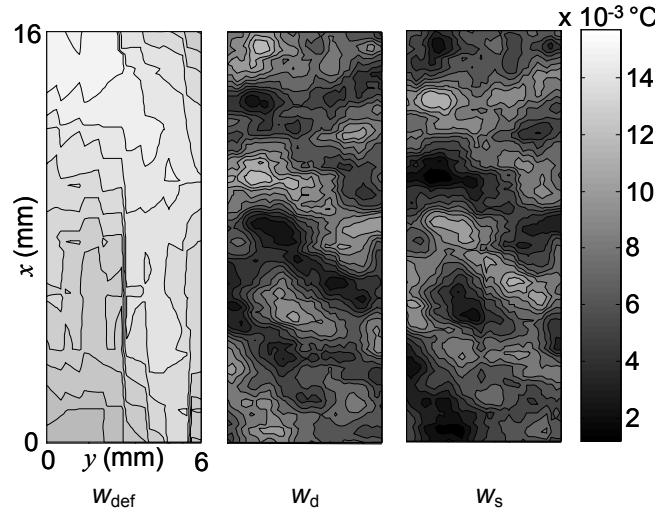


Fig. 3: Fields of the mean energy balance associated with a cycle of block #11.

An initial overview of Figure 3 shows that the mean deformation energy over a cycle (around $14 \times 10^{-3} \text{ °C}$) is roughly made of 50% of dissipated energy and 50% of stored energy. At this level we ought to mention the work of Kaleta [16], which showed similar results at the specimen scale. While studying a ferritic-perlitic steel, he observed stored energy ratios associated with the stress-strain hysteresis loop varying from 37.4% for low cycle fatigue tests (LCF), and up to 67.3% for high cycle fatigue tests (HCF). In aluminium alloys, stored energy ratios were estimated from 0.1 to 0.2 in other works [17, 18].

An accurate observation of Figure 3 shows a more complicated situation induced by a heterogeneous distribution of the different energies. We already underlined the non uniformity of the dissipation fields induced by HCF [4]. Here, the dissipated and stored energy vary in an initial close approximation between $4 \times 10^{-3} \text{ °C}$ and $8 \times 10^{-3} \text{ °C}$.

The last point we would like to mention is related to the comparison between both energy balances. We can observe that patterns of dissipated and stored energy are very similar. These patterns are of prime interest since high dissipation zones represent potential zones where a fatigue crack may occur [4].

5 □ CONCLUDING COMMENTS

In this paper, we presented a combined application of DIC and IRT to the fatigue of DP 600 steel. We used kinematic and thermal data to estimate the deformation energy and the mean dissipated energy per cycle. The deformation energy distribution was computed using strain field measurements, while the stress fields were estimated using a variational inverse method. The heat source distributions were derived from thermal data using a local expression of the heat equation. The linearity of the diffusion equation and that of the thermal boundary conditions enabled us to estimate the sources separately. Finally, 2D identified fields obtained with DP 600 steel specimen were presented. The analysis did not reveal any noticeable influence of high cycle fatigue on the elastic properties (test limited to around 1.5×10^5 cycles). We also observed that the distribution of mean deformation energy rates per cycle was relatively homogeneous while the image processing showed that dissipation localized since the very beginning of the test. The quasi-homogeneity of the volume deformation energy is observed at the scale imposed by the optical systems and the image processing. It seems to be quite natural since stress and strain gradients should theoretically vanish at this scale for a uniform cyclic tensile test. The heterogeneous distribution of dissipation is not totally surprising since we admit that the persistent slip bands (PSB) develop gradually in some favorably oriented grains. The wavelength spectrum of the measured distribution seems to be such that the change of scale corresponding to our observation is not sufficient to make an averaged value representative of the distribution. Consequently, the observed distribution of dissipation remains heterogeneous,

the high dissipation zones corresponding to high concentrations of PSB. Furthermore, image processing showed that the amounts of deformation energy corresponding to the stress-strain hysteresis loop were equally stored and dissipated. This finding could obviously have a marked impact on the modeling of steel fatigue kinetics, so these preliminary results must, as usual, be considered with precaution. Complementary checks and tests should be performed in the near future. Nevertheless, the benefit of combining DIC and IRT measurement to perform local energy balance was here highlighted. Such approaches show a promising potential for the in depth characterization of steel fatigue.

Acknowledgments

The authors would like to thank Arcelor Research SA and Nippon Steel Corporation for their technical and financial support during this study. The authors, members of LMGC, would also like to warmly thank the Arcelor Fatigue Working Group for the fruitful and animated scientific discussions.

References

1. Luong, M. P. (1998) Fatigue limit evaluation of metals using an infrared thermographic technique. *Mech. of Mat.*, 28,155-163.
2. La Rosa, G. and Risitano, A. (2002) Thermographic methodology for rapid determination of the fatigue limit of materials and mechanical components. *Int. J. of Fatigue*, 22, 1, 65-73.
3. Cugy, P. and Galtier, A. (2002) Microplasticity and temperature increase in low carbon steels. *Proc. 8th Int. Fatigue Conference, Stockholm*, 549-556
4. Boulanger, T., Chrysochoos, A., Mabru, C. and Galtier, A. (2004) Calorimetric and thermoelastic effects associated with the fatigue behavior of steels. *Int. J. of Fatigue*, 26, 221-229
5. Wattrisse, B., Chrysochoos, A., Muracciole, J.-M. and Nemoz-Gaillard, M. (2000) Analysis of strain localisation during tensile test by digital image correlation. *J. of Exp. Mech.*, 41, n° 1, 29-38.
6. Berthel, B., Chrysochoos, A., Wattrisse, B. and Galtier, A., (2007), Infrared image processing of the calorimetric analysis of fatigue phenomena, *J. of Exp. Mech.*, in press (on line).
7. Germain, P, Nguyen, Q. S. and Suquet, P. (1983) Continuum thermodynamics. *J. of Applied Mechanics*, 50, 1010-1020.
8. Geymonat, G., Hild, F. and Pagano S. (2002) Identification of elastics parameters by displacement field measurement. *C.R. Mécanique*, 330, 403-408
9. Latourte, F., Chrysochoos, A., Pagano S., Wattrisse, B. (2007) Elastoplastic behavior identification for heterogeneous loadings and materials, *J. of Exp. Mech.*, 48, 435-449.
10. Chrysochoos, A., Berthel, B., Latourte, F., Pagano, S., Wattrisse, B., Weber, B., (2008), Local energy approach to steel fatigue, *Strain*, 44, 327-334.
11. Berthel, B., Galtier, A., Wattrisse, B. and Chrysochoos A. (2007), Fatigue dissipation properties of steel sheets. *Strain: an int. J. for Exp. Mech.*, 43 (3), 273-279.
12. Morabito, A.E., Chrysochoos, A., Dattoma, V., Galietti, U., (2007); Analysis of heat sources accompanying the fatigue of 2024 T3 aluminium alloys, *Int. J. of Fatigue*, 29, 977-984.
13. Chrysochoos, A. Berthel, B., Latourte, F., Galtier, A., Pagano, S., and Wattrisse, B., (2008) Local energy analysis of high-cycle fatigue using digital image correlation and infrared thermography, *J. of Strain Analysis for Engng. Design*, 43(6), 411-422.
14. Doudard, C., Hild, F. and Calloch, S., (2007), A probabilistic model for multiaxial high cycle fatigue, *Fat. Frac. Engng. Mat. Struct.*, (30), 107-114.
15. Doudard, C., Poncelet, M., Calloch, S., Boué, C., Hild, F. and Galtier, A., (2007), Determination of an HCF criterion by thermal measurements under biaxial cyclic loading, *Int. J. Fat.*,(29), 748-757.
16. Kaleta, J. (1998) Determination of cold work energy in LCF/HCF region. *Proc. of 4th Int. Conf. on LCF and Elasto-Plastic Behaviour of Materials, Garmisch-Partenkirchen*, 93-98.
17. Wong, A. K. and Kirby III, G. C. (1990) A hybrid numerical/experimental technique for determining the heat dissipated during low cycle fatigue. *Engng Frac. Mech.*, 37, 3, 493-504.
18. Harvey II, D. P. and Bonenberger Jr, R. J. (2000) Detection of fatigue macrocracks in 1100 aluminium from thermomechanical data. *Engng Frac. Mech.*, 65, 609-6